Electric field induced large Rashba effect and topological phase transition in halide perovskite superlattices

Xinyu Wang, Xu Li, Hao Tian, Hai Sang, Jian Zhou, Lan Chen, Hong Jian Zhao, Di Wu, Haijun Zhang, Laurent Bellaiche, Jun-Ming Liu, and Yurong Yang

Phys. Rev. B **108**, 045114 — Published 11 July 2023

DOI: 10.1103/PhysRevB.108.045114

Electric field induced large Rashba effect and topological phase transition in halide perovskite superlattices

Xinyu Wang[1,2], Xu Li[1,2], Hao Tian[3], Hai Sang[1], Jian Zhou[1,2], Lan Chen[1,2,4], Hong Jian Zhao[4], Di Wu[1,2], Haijun Zhang[1], Laurent Bellaiche[5], Jun-Ming Liu[1], Yurong Yang[1,2,*]

[1]*Laboratory of Solid State Microstructures, Nanjing University, Nanjing 210093, China*

[2]*Jiangsu Key Laboratory of Artificial Functional Materials, Department of Materials Science and Engineering, Nanjing University, Nanjing 210093, China*

[3]*School of Physics and Electronic Engineering, Zhengzhou Normal University, Zhengzhou, 450044, China*

[4]*Nantong Institute of Material Engineering Technology, Nanjing University, Nantong, China*

5International Center for Computational Method and Software, College of Physics, Jilin University, Changchun 130012, China

[6]*Physics Department, Institute for Nanoscience and Engineering, University of Arkansas, Fayetteville, Arkansas 72701, USA*

Abstract: We introduce superlattices made of ferroelectric halide perovskites as a new class of functional materials possessing large Rashba effect and phase transition from normal insulator to topological insulator induced by electric field. Using first-principles methods, in $CsPbI_3/CsSiI_3$ and $CsSnI_3/CsSiI_3$ superlattices we found a non-monotonic Rashba parameter with respect to the magnitude of polarization and large maximal Rashba effect at a critical polarization, where the phase transition from normal insulator to topological insulator occurs when changing the polarization. This phase transition and the large maximal Rashba effect are related to bandgap engineering under electric field. In contrast to traditional non-polar topological insulator, in these ferroelectric topological insulators the energy level of the Dirac point and the spin texture of surface states are largely tunable by changing polarization or strain. Our results thus highlight the interplay among ferroelectricity, Rashba effect, and

* Electronic mail: yangyr@nju.edu.cn

topological order in a single material, which is promising towards electronic and spintronic applications.

Topological insulator states [1-5] and Rashba-type effects [6-10] are among the most interesting current phenomena in condensed matter physics, as a result of relativistic interaction of spin-orbit coupling (SOC). Topological insulators, exhibiting robust edge/surface currents and spin-momentum locking, provide platforms for various fundamental exciting research, including magnetic monopoles [11], Majorana fermions [12], and the application of fault-tolerant quantum computing [13,14]. Bulk Rashba-type spin splitting, which occurs in materials/interface with breaking spatial inversion symmetry, can lead to spin-Hall effect [15-17], spin interference [18,19], and spin-to-charge current interconversions [20,21]. Both topological phase and Rashba effects present strong spin-momentum locking, in principle, providing a possibility of electric field control of electronic spins by manipulating topological order and Rashba effects. Ferroelectric materials are ideal candidates for controlling the topological order and Rashba effects via electric field. Recently, linear Rashba effect with polarization has been extensively discovered in ferroelectrics[22-25]. Promisingly, topological order can also exist in ferroelectrics, for example, the hexagonal ABC hyperferroelectrics, antiferroelectrics [26,27], and the heterostructures consisting of topological insulators and ferroelectrics [28-30]. These discoveries highlight the possibility of simultaneously controlling Rashba effect and topological state by electric field in a non-volatile way in ferroelectrics. On the other hand, the ferroelectric materials possessing topological order discovered recently are non-perovskite structures. In the prototypical ferroelectric perovskite structure for which the designing and producing technology have been well developed, the topological orders have never been measured and therefore simultaneously tuning the topological order and Rashba effect by electric field has not been realized either, to the best of our knowledge. One therefore still needs to find possible materials hosting simultaneously Rashba effects and topological order, and that are tunable by electric field.

Iodide perovskites (ABI_3) are candidates for that, since they hold large SOC due to the heavy element of iodine and ferroelectric properties as a result of perovskites having the

possibility to be ferroelectrics [31-38]. Both $CsPbI_3$ and $CsSnI_3$ adopt the *Pnma* perovskite phase for their ground state with in-plane antipolar distortion [39,40]. On the other hand, the ground state of $CsSiI_3$ adopts a perovskite structure with *R3m* symmetry [22,41-43]. One can easily imagine that the perovskite $CsPbI_3/CsSiI_3$ and $CsSnI_3/CsSiI_3$ superlattices will possess structural distortion with either *Pnma* or/and *R3m* type distortion. We thus investigated the short-period [1/1] iodide perovskite superlattices made of $CsPbI_3/CsSiI_3$ and $CsSnI_3/CsSiI_3$ by first-principles. These superlattices are indeed found to possess a large Rashba effect, which even shows an anomalous behavior with the change of polar distortion. A transition from normal insulator (NI) to topological insulator (TI) by electric field is also presently predicted, along with a large Rashba effect at the critical field for which the NI to TI transition occurs. Moreover, the Dirac point in bulk bandgap can be shifted by electric field and strain, even crossing the Fermi level. Consequently, the spin texture of the surface state is tunable by electric field. Our results therefore provide a powerful and convenient way to tune topological order and Rashba effect.

Density functional theory (DFT) calculations are performed using the Vienna *ab initio* simulation package (VASP) with the projector augmented wave (PAW) method [44,45]. An energy cutoff of 320 eV, a *k*-point grid size of $8 \times 8 \times 6$, and the Perdew-Burke-Ernzerhof parametrization revised for solids (PBEsol) functional [46] are used in all the calculations. We further performed calculations using the HSE hybrid functional [47] to confirm the robustness of the PBEsol functional in the supplemental materials [48]. Atomic structural relaxations are carried out until the force on each atom was less than 0.001 eV $Å^{-1}$ and the energy convergence criteria of 10^{-8} eV was adopted. The calculations are performed in the iodide perovskite superlattices of $[CsPbI_3]_1/[CsSiI_3]_1$ and $[CsSnI_3]_1/[CsSiI_3]_1$, where one-unit layer of $CsSiI_3$ and one unit layer of $CsPbI_3$ or $CsSnI_3$ successively alternate along the pseudocubic [001] direction (see Fig. 1). A supercell with 20 atoms is used in DFT calculations, in which the lattice vectors are $\boldsymbol{a}=a(\boldsymbol{x}+\boldsymbol{y})$, $\boldsymbol{b}=b(-\boldsymbol{x}+\boldsymbol{y})$ and $\boldsymbol{c}=c\boldsymbol{z}$, where the *a*, *b*, and *c* are related to the magnitude of the lattice constants and $\boldsymbol{x}$, $\boldsymbol{y}$ are $\boldsymbol{z}$ are unit vectors along the pseudocubic [100], [010] and [001] directions, respectively. Ferroelectric polarizations are calculated by using Born effective charge and atomic displacements. Tight-binding analysis with the WANNIER90 package was further performed for the calculation of

topological phases [49,50]. The *s*- and *p*-orbital basis was used to construct the tight-binding Hamiltonian, and the topological indices were calculated by tracking hybrid Wannier charge centers using the WannierTools package [51].

The calculations confirm that the $CsPbI_3/CsSiI_3$ with space group of $P2_1$ and $CsSnI_3/CsSiI_3$ with space group of *Pc* both possess an octahedral tilting type of $a^-a^-c^+$ pattern (using Glazer notation [52]) with out-of-phase in-plane octahedral tilting and in-phase of out-of-plane octahedral tilting [see Figs. S1(a) and (b)], and in-plane polar distortion (Q_{P_b}) with B-sites cations moving along the ***b*** direction while I anions move along the ***a*** and ***b*** directions [see Fig. 1(b)]. The in-plane polarization for $CsPbI_3/CsSiI_3$ and $CsSnI_3/CsSiI_3$ is found to be 16.1 μC/cm^2 and 12.3 μC/cm^2, respectively. The major structural difference between $CsPbI_3/CsSiI_3$ and $CsSnI_3/CsSiI_3$ is that the latter additionally possesses another polar distortion along the ***c*** direction [Q_{P_c}, see Fig. S1(c)], with a polarization of 8.2 μC/cm^2, as similar to the structure of $BiInO_3$ [53]. The structural similarity of iodine octahedral tilting and in-plane polarization in the two superlattices may lead to some electrical properties being similar.

Because of the polar symmetry and the large SOC associated with the heavy elements of I and Sn, the electronic structure of this superlattice shows that Rashba-type splittings occur along the Γ-B line in the Brillouin zone [see Fig 2(a)]. The Rashba energy for the highest valence bands (HVB) is 6.3 meV and it is 12.7 meV for the lowest conduction bands (LCB). The Rashba parameter ($\alpha_R = 2E_R/k_0$) of HVB and LCB is 1.38 and 1.44 eVÅ, respectively. The bandgap for $CsSnI_3/CsSiI_3$ is rather small (*i.e.*, 48 meV). Such a small gap can likely be engineered to vanish [54] by changing the polarization. Therefore, it is legitimate to wonder whether such a gap closing (if it occurs) can be accompanied by a topological transition.

Figures 2(b) and (c) show the band structures of $CsSnI_3/CsSiI_3$ with the reduced in-plane polarization (P_b) of 7.4 μC/cm^2 and 0, respectively (the structures with reduced polarization are constructed by reducing the magnitude of the polar mode Q_{P_b}). As shown in Fig. 2, one can see that the bandgap indeed decreases from 48 meV to zero when the polarization decreases from 12.3 to 7.4 μC/cm^2, and then reopens when the polarization is smaller than 7.4 μC/cm^2. The bandgap increases to 50 meV when P_b further decreases to zero. In the band

structure of $CsSnI_3/CsSiI_3$ with P_b larger than 7.4 μC/cm^2 (see Fig. 2(a)), the highest valence bands near the Γ point are dominated by I-*5p* states, while the conduction bands near the Fermi level are mainly from B-site (Sn-*5p* and Si-*3p*). In contrast, the highest valence bands at the Γ point come from the B-site (Sn-*5p* and Si-*3p*) while the third lowest conduction bands at Γ point are dominated by I-*5p* states when the polarization is smaller than 7.4 μC/cm^2 [see Fig. 2(c)]. These band structures clearly show a band inversion induced by decreasing the in-plane polarization. Thus, the NI-TI transition of $CsSnI_3/CsSiI_3$ occurs when the polarization is smaller than 7.4 μC/cm^2. To further confirm this TI state, we calculated the topological invariant $\mathbb{Z}_2$ which is (1;000), thus indicating that it is indeed a strong topological insulator.

We then consider the Rashba effect of the studied superlattices when changing the polarization. Figure 3 displays the Rashba parameters and bandgaps as a function of polarization P_b in $CsPbI_3/CsSiI_3$ and $CsSnI_3/CsSiI_3$ superlattices. The bandgap of $CsPbI_3/CsSiI_3$ monotonically decreases from 180 to 60 meV when decreasing the polarization from 16.1 to 0 μC/cm^2. It is consistent with the fact that the polar distortion (polarization) of perovskite structure widens its bandgap by allowing band edge orbitals to mix and repel each other [55,56]. Rashba parameters first increase from 0.2 to 1.2 eVÅ for HVB, and from 0.05 to 1.3 eVÅ for LCB, respectively, when decreasing the polarization from 16.1 to 3.3 μC/cm^2. As the polarization further decreases to zero, Rashba parameters of both HVB and LCB sharply decrease to zero. This non-monotonic phenomenon of Rashba parameters with respect to polarization is different from those reported in the literature where the Rashba parameter is linear with polarization (as found for GeTe, BrF_5, $BiAlO_3$ and $SrTiO_3$ [23-25,57]). We construct an effective two-band Hamiltonian with respect to *P2₁* space group (around the Γ point of the Brillion Zone), incorporating various degrees of freedom, namely, the electronic polarization P_b (*i.e.*, along the *y* direction), electronic momentum k_α (α = *x*, *y*, *z*), and electronic spin characterized by the Pauli matrices σ_β (β = *x*, *y*, *z*). The Hamiltonian is written as $H_R = E_0 + \lambda_{xx}k_x\sigma_x + \lambda_{xz}k_x\sigma_z + \lambda_{yy}k_y\sigma_y + \lambda_{zx}k_z\sigma_x + \lambda_{zz}k_z\sigma_z$. The corresponding eigenvalue and spin splitting magnitude are given by: $E_R = E_0 \pm \sqrt{(\lambda_{xx}k_x + \lambda_{zx}k_z)^2 + \lambda_{yy}k_y)^2 + (\lambda_{xz}k_x + \lambda_{zz}k_z)^2}$, where $\lambda_{\alpha\beta}$ (α, β = *x*, *y*, *z*) are

parameters characterizing spin splitting terms, $\lambda_{\alpha\beta} = \lambda_{\alpha\beta 1} P_{\mathrm{b}} + \lambda_{\alpha\beta 3} P_{\mathrm{b}}^3 + \lambda_{\alpha\beta 5} P_{\mathrm{b}}^5 + \cdots$). Figures S4 (a)-(c) show the band structures around the Γ point along k_{x}, k_{z} and k_{y}, respectively. Our model coincides with the band structures from DFT calculations. The phenomena of Rashba parameters evolve in a nonlinear manner with respect to the polarization P_{b} indicate that the $\lambda_{\alpha\beta 3}$ and $\lambda_{\alpha\beta 5}$ coefficients are not negligible in halide superlattice, unlike the situation of various conventional Rashba materials. As a matter of fact, the non-monotonic behavior can also be understood from the special in-plane polar mode in the superlattice. As shown in Fig. 1(b), the in-plane polar mode $\mathrm{Q}_{P_{\mathrm{b}}}$ can be decomposed into two components, $\mathrm{Q}_{P_{\mathrm{b},||}}$ and $\mathrm{Q}_{P_{\mathrm{b},\perp}}$ that are associated with atomic motions being parallel and perpendicular to the ***b*** direction, respectively. Both $\mathrm{Q}_{P_{\mathrm{b},||}}$ and $\mathrm{Q}_{P_{\mathrm{b},\perp}}$ contribute to the in-plane polarization along the ***b*** direction, as well as, to the Rashba effect. $\mathrm{Q}_{P_{\mathrm{b},||}}$ gives rise to a negative Rashba parameter while $\mathrm{Q}_{P_{\mathrm{b},\perp}}$ results in a positive one (see Fig. S4). These two opposite contributions yield a non-monotonic behavior of the total Rashba parameter with respect to the polarization.

Figure 3(b) shows the bandgap and Rashba parameters of $CsSnI_3/CsSiI_3$ as a function of polarization P_{b}. The bandgap first decreases to zero when P_{b} decreases from 12.3 to 7.4 μC/cm^2, and then reopens from 0 to about 50 meV when further decreasing P_{b} from 7.4 μC/cm^2 to 0. At P_{b}=7.4 μC/cm^2, the NI-TI phase transition occurs (also see Fig. 2) and TI states for P_{b} smaller than 7.4 μC/cm^2 are strong TI with topological invariant $\mathbb{Z}_2$ of (1;000). The Rashba parameters of $CsSnI_3/CsSiI_3$ show a non-monotonic behavior as a function of the polarization. The maximum of Rashba parameters is about 6 eVÅ at the critical polarization, thus enhanced three times as compared to the Rashba parameter of the superlattice without reducing polarization, and comparable to the largest Rashba parameter of 6.8 eVÅ in SnTe reported in literatures [58]. This increase of the Rashba parameter not only comes from the competition between the contributions of the two components of the polar modes [Fig. S4], but also to the fact that the HVB and LCB are symmetrically of the same character, and therefore very effectively couple with each other through a Rashba-type Hamiltonian [59,60],

$\Delta\varepsilon_m(\mathbf{k}) = \frac{\hbar}{m_0}\sum_{n\neq m}\frac{\langle u_m|H|u_n\rangle\langle u_n|\mathbf{q}\cdot\mathbf{p}|u_m\rangle + c.c.}{\varepsilon_m-\varepsilon_n}$, where u_i and ε_i are the eigenstate and eigenenergy corresponding to the state i at $\mathbf{k_0}$, respectively, $\mathbf{q}=\mathbf{k}-\mathbf{k_0}$, $\mathbf{p}$ denotes the momentum operator, H is the corresponding Hamiltonian for Rashba-type-splitting, and *c.c.* stands for complex conjugate. Therefore, the spin-splitting clearly depends on the energy difference between the state m and its neighboring state n. In the band structure of $CsSnI_3/CsSiI_3$, the state m can be HVB or LCB. The energy difference (ε_m-ε_n) between the m state (HVB or LCB) and its neighboring states decreases and $\Delta\varepsilon_m$ thus increases. At the critical polarization for which the bandgap is closed, $\varepsilon_m - \varepsilon_n$ is almost zero and their Rashba splitting reaches its maximum.

We now consider the surface state of TI phase in $CsSnI_3/CsSiI_3$ superlattice. The energy variation of $CsSnI_3/CsSiI_3$ superlattice along the path connecting the noncentrosymmetric to centrosymmetric direction show a low ferroelectric switching barrier (in Fig. S2), indicating that the ferroelectric polarization can be switched by electric field. Figures 4(a)-(c) show the band structures and corresponding spin textures of surface states for P_b=6.1, 0, and -6.1 μC/cm^2, respectively. There are two nonequivalent Dirac cones which come from the Sn/Si-I termination and Cs-I termination (100) surface of the geometry slab, which contrast with the degenerate Dirac points in non-polar TI structures [2,3,61]. For the case of P_b=6.1 μC/cm^2 shown in Fig. 4(a), the Dirac point from Cs-I termination (red color) is above the Fermi level and buried in the continuum of bulk conduction states. The Dirac point from Sn/Si-I termination (blue color) is below the Fermi level. Spin textures of the two surfaces states show the same chirality [bottom panel of Fig. 4(a)]. For the superlattice with zero polarization, the surface bands and Dirac points shift to higher energy, as compared to the case of P_b=6.1 μC/cm^2 [Fig. 4(b)]. Both Dirac points from Cs-I and Sn/Si-I termination are above the Fermi level, leading to the opposite chirality of spin texture of the surface states [bottom panel of Fig. 4(b)]. For the superlattice with P_b=−6.1 μC/cm^2 [Fig. 4(c)], the surface bands shift to lower energy as compared to the case of P_b=0 and the Dirac point of Sn/Si-I termination is below the Fermi level. Similar to the case of P_b=6.1 μC/cm^2, for P_b=−6.1 μC/cm^2 one Dirac point (from Cs-I termination surface) is above the Fermi level and the other Dirac point (from Sn/Si-I termination surface) is below the Fermi level. While different

from the case of P_b=6.1 μC/cm^2, for P_b=−6.1 μC/cm^2 the surface bands from Sn/Si-I termination (blue color) is much more flat, leading to them to be the outer branch bands and the surface bands from Cs-I termination become the inner branch bands at the Fermi level. Interestingly, in the superlattices with opposite direction of polarization, the chirality of spin texture of surface states is the same, though the inner and outer branches of surface bands differ, as a result of a difference in the surface termination [see the bottom panels of Fig. 4(a) and (c)]. Furthermore, the same chirality of the spin texture of surface states in the phases with opposite direction of polarization contrasts with the spin texture of states of Rashba effects, where the chirality is reversed when the polarization is switched [see Figs. 4(e) and (f)] [26,27,62-64].

Figure 4(d) further shows the energy of the Dirac point as a function of polarization. The energy of the Dirac point from Cs-I termination surface is always above the Fermi level, while that from Sn/Si-I termination is above the Fermi level for polarization ranging between −4.7∼4.7 μC/cm^2, and is below the Fermi level for polarization larger in magnitude than 4.7 μC/cm^2. Therefore, the energy level of Dirac point and the chirality of spin texture are dependent on the magnitude and direction of polarization. Note that one I ions in Cs-I termination surface has one nearest neighboring Sn/Si ion, while one Sn/Si ion of Sn/Si-I termination surface has five neighboring I ions. From the tight-binding model, the transfer integral of the states from Cs-I termination surface is much smaller than that from Sn/Si-I termination surface, leading to the surface states from Sn/Si-I termination largely shifting their energy while that of Cs-I termination slightly change their energy when changing the polarization. This electric field control of the Dirac point position in the bandgap and altogether with the chirality of spin texture of the surface state therefore provides a powerful and convenient toolkit to manipulate topological properties in ferroelectric perovskite.

Different from $CsSnI_3/CsSiI_3$ where a NI-TI phase transition occurs by reducing the polarization, $CsPbI_3/CsSiI_3$ is always NI in the whole range of polarization [see Fig. 3(a)] since it has a larger bandgap (180 meV) than $CsSnI_3/CsSiI_3$ (48 meV). We now employ the epitaxial strain to engineer the bandgap of superlattices. Figure 5 displays the bandgap of $CsPbI_3/CsSiI_3$ and $CsSnI_3/CsSiI_3$ as a function of such strain. The superlattices is NI (light blue color in Fig. 5) where the bandgap decreases with the decrease of the strain from a

tensile strain of 2% to -2.7% for $CsPbI_3/CsSiI_3$ and from 2% to -0.8% for $CsSnI_3/CsSiI_3$. At the strain range from -1.8% and -2.7% for $CsPbI_3/CsSiI_3$, and from 2% and -0.8% for $CsSnI_3/CsSiI_3$, the bandgap is small and the phase NI can transform to phase TI by decreasing the polarization (phase TI-E, blue color in Fig. 5). At the critical strains where the bandgaps for both superlattices are zero, the structures become Weyl semimetals. When the strain is smaller than the critical strain, the superlattices are TI phase (green color in Fig. 5). Additionally, $CsSnI_3/CsSiI_3$ becomes a NI phase [light blue color in Fig. 5(b)] at the large compressive strain from -3.5% to -4% in Fig 5(b).

Note that the energy of Dirac points of TI phases can be changed and even crosses the Fermi level when the strain changes. Figure 5(c) displays the energy of Dirac point of the TI phase in $CsPbI_3/CsSiI_3$ and $CsSnI_3/CsSiI_3$ as a function of strain. For $CsPbI_3/CsSiI_3$, both Dirac points shift to lower energy when increasing the magnitude of compressive strain. Moreover, the energy of Dirac point coming from the Pb/Si-I surface shifts from above the Fermi level to below the Fermi level, and thus crosses the Fermi level. This shift of Dirac points is related to the change of Pb-I and Si-I bonds and the transfer integral between Pb/Si and I in the tight-binding model. For $CsSnI_3/CsSiI_3$, the Dirac point from Cs-I termination decreases with the increase of magnitude of compressive strain, and cross the Fermi level at strain -3%. Contrarily, the Dirac point from Sn/Si-I termination increases with the increase of magnitude of compressive strain, and cross the Fermi level at strain -2.3%. The shift of two Dirac energy level of $CsSnI_3/CsSiI_3$ is not only dependent on the length of Sn-I/Si-I bonds but is also related to the polarization along the *b* and *c* directions. The polarization along the *b* direction decreases and the polarization along the *c* direction increases when increasing the magnitude of compressive strain (see Fig. S11). At strain about -2.5%, the polarizations along *b* and along *c* directions are equal to each other, which may lead to similar energies of the Dirac points from Cs-I and Sn/Si-I terminations. Similar to the effect of polarization on the surface states in the TI-E phase [see Fig. 4(d)], the strain can shift the energy of the Dirac point and revert the chirality of spin texture of surface states at the Fermi level. This topological phase and tunable surface states provide a novel and convenient route to tune the topological order.

In summary, we predicted a large Rashba effect and electric field induced topological order in halide perovskite superlattices of $CsPbI_3/CsSiI_3$ and $CsSnI_3/CsSiI_3$. A non-monotonic behavior of Rashba parameter as a function of polarization is found and a large Rashba parameter can be achieved at a critical polarization where the NI-TI phase transition occurs. Moreover, in the TI phase, the spin texture of surface states and Dirac point energy are tunable by changing the polarization under electric field. The discovery of new class of ferroelectric with transition between NI and TI states and tunable Rashba effect broaden the potential application of topological properties in electronics and spintronics.

Acknowledgments. The authors thank the National Key R&D Program of China (grant No. 2022YFB3807601, 2020YFA0711504), the National Science Foundation of China (grant Nos. 12274201, 12274174, 51725203, 51721001, 52003117) and the Natural Science Foundation of Jiangsu Province (grant No. BK20200262). We are grateful to the HPCC resources of Nanjing University for the calculations. L.B. thanks the Vannevar Bush Faculty Fellowship (VBFF) Grant No. N00014-20-1-2834 from the Department of Defense.

References

[1] B. A. Bernevig, T. L. Hughes, and S.-C. Zhang, Science **314**, 1757 (2006).

[2] Y. Chen, J. G. Analytis, J.-H Chu, Z. Liu, S.-K. Mo, X.-L. Qi, H. Zhang, D. Lu, X. Dai, Z. Fang *et al*., Science **325**, 178 (2009).

[3] H. Zhang, C.-X. Liu, X.-L. Qi, X. Dai, Z. Fang, and S.-C. Zhang, Nat. Phys. **5**, 438 (2009).

[4] Z. Zhu, Y. Cheng, and U. Schwingenschlögl, Phys. Rev. Lett. **108**, 266805 (2012).

[5] A. Edström, D. Amoroso, S. Picozzi, P. Barone, and M. Stengel, Phys. Rev. Lett. **128**, 177202 (2022).

[6] N. S. Averkiev and L. E. Golub, Phys. Rev. B **60**, 15582 (1999).

[7] A. Manchon, H. C. Koo, J. Nitta, S. M. Frolov, and R. A. Duine, Nat. Mater. **14**, 871 (2015).

[8] H. Djani, A. C. Garcia-Castro, W. Y. Tong, P. Barone, E. Bousquet, S. Picozzi, and P. Ghosez, Npj Quantum Mater. **4**, 1 (2019).

[9] K. Rubi, J. Gosteau, R. Serra, K. Han, S. W. Zeng, Z. Huang, B. Warot-Fonrose, R. Arras, E. Snoeck, Ariando M. Goiran, W. Escoffier *et al*., Npj Quantum Mater. **5**,1 (2020).

[10] K. Yamauchi, P. Barone, and S. Picozzi, Phys. Rev. B **100**, 245115 (2019).

[11] X.-L. Qi, R. Li, J. Zang, and S.-C. Zhang, Science **323**, 1184 (2009).

[12] L. Fu and C. L. Kane, Phys. Rev. Lett. **100**, 096407 (2008).

[13] M. Konig, S. Wiedmann, C. Brune, A. Roth, H. Buhmann, L. W. Molenkamp, X.-L. Qi, and S.-C. Zhang, Science **318**, 766 (2007).

[14] I. Knez, R.-R. Du, and G. Sullivan, Phys. Rev. Lett. **107**, 136603 (2011).

[15] J. E. Hirsch, Phys. Rev. Lett. **83**, 1834 (1999).

[16] J. Sinova, S. O. Valenzuela, J. Wunderlich, C. H. Back, and T. Jungwirth, Rev. Mod. Phys. **87**, 1213 (2015).

[17] I. Sodemann, Z. Zhu, and L. Fu, Phys. Rev. X **7**, 041068 (2017).

[18] J. Nitta, F. E. Meijer, and H. Takayanagi, Appl. Phys. Lett. **75**, 695 (1999).

[19] D. Frustaglia and K. Richter, Phys. Rev. B **69**, 235310 (2004).

[20] K. Kondou, R. Yoshimi, A. Tsukazaki, Y. Fukuma, J. Matsuno, K. Takahashi, M. Kawasaki, Y. Tokura, and Y. Otani, Nat. Phys. **12**, 1027 (2016).

[21] S. Manipatruni, D. E. Nikonov, C.-C. Lin, T. A. Gosavi, H. Liu, B. Prasad, Y.-L. Huang, E. Bonturim, R. Ramesh, and I. A. Young, Nature **565**, 35 (2019).

[22] D. Liu, Q. Li, H. Jing, and K. Wu, J. Phys. Chem. C **123**, 3795 (2019).

[23] P. Noël, F. Trier, L. M. Vicente Arche, J. Bréhin, D. C. Vaz, V. Garcia, S. Fusil, A. Barthélémy, L. Vila, M. Bibes *et al.*, Nature **580**, 483 (2020).

[24] C. M. Acosta, A. Fazzio, G. M. Dalpian, and A. Zunger, Phys. Rev. B **102**, 144106 (2020).

[25] L. G. D. da Silveira, P. Barone, and S. Picozzi, Phys. Rev. B **93**, 245159 (2016).

[26] D. Di Sante, P. Barone, A. Stroppa, K. F. Garrity, D. Vanderbilt, and S. Picozzi, Phys. Rev. Lett. **117**, 076401 (2016).

[27] B. Monserrat, J. W. Bennett, K. M. Rabe, and D. Vanderbilt, Phys. Rev. Lett. **119**, 036802 (2017).

[28] Z. Zheng, Q. Ma, Z. Bi, S. de La Barrera, M.-H. Liu, N. Mao, Y. Zhang, N. Kiper, K. Watanabe, T. Taniguchi *et al.*, Nature **588**, 71 (2020).

[29] S. Chen, S. Yuan, Z. Hou, Y. Tang, J. Zhang, T. Wang, K. Li, W. Zhao, X. Liu, L. Chen *et al.*, Adv. Mater. **33**, 2000857 (2021).

[30] D. Doennig, W. E. Pickett, and R. Pentcheva, Phys. Rev. B **89**, 121110(R) (2014).

[31] Y. Zhai, S. Baniya, C. Zhang, J. Li, P. Haney, C.-X. Sheng, E. Ehrenfreund, and Z. V. Vardeny, Sci. Adv. **3**, e1700704 (2017).

[32] E. Lafalce, E. Amerling, Z.-G. Yu, P. C. Sercel, L. Whittaker-Brooks, and Z. V. Vardeny, Nat. Commun. **13**, 1 (2022).

[33] J. Kaur and S. Chakraborty, ACS Appl. Energy Mater. **5**, 5579 (2022).

[34] X. Zhou and Z. Zhang, AIP Adv. **10**, 085210 (2020).

[35] L. Leppert, S. E. Reyes-Lillo, and J. B. Neaton, J. Phys. Chem. Lett. **7**, 3683 (2016).

[36] H. Jin, J. Im, and A. J. Freeman, Phys. Rev. B **86**, 121102(R) (2012).

[37] R. Kashikar, B. Khamari, and B.R.K. Nanda, Phys. Rev. Mater. **2**, 124204 (2018).

[38] X. Y. Wang, X. Li, H. Tian, H. Sang, J.-M. Liu, and Y. Yang, J. Phys. Chem. C **126**, 20620 (2022).

[39] R. J. Sutton, M. R. Filip, A. A. Haghighirad, N. Sakai, B. Wenger, F. Giustino, and H. J. Snaith, ACS Energy Lett. **3**, 1787 (2018).

[40] T. Ye, X. Wang, K. Wang, S. Ma, D. Yang, Y. Hou, J. Yoon, K. Wang, and S. Priya, ACS Energy Lett. **6**, 1480 (2021).

[41] Z. Fang, M. Shang, X. Houa, Y. Zheng, Z. Du, Z. Yang, K.-C. Choua , W. Yang, Z. L. Wang, and Y. Yang, Nano Energy **61**, 389 (2019).

[42] S. K. Radha, C. Bhandari, and W. R. L. Lambrecht, Phys. Rev. Mater. **2**, 063605 (2018).

[43] L. Y. Huang and W. R. L. Lambrecht, Phys. Rev. B **93**, 195211 (2016).

[44] P. E. Blöchl, Phys. Rev. B **50**, 17953 (1994).

[45] G. Kresse and J. Furthmüller, Comput. Mater. Sci. **6**, 15 (1996).

[46] J. P. Perdew, A. Ruzsinszky, G. I. Csonka, O. A. Vydrov, G. E. Scuseria, L. A. Constantin, X. Zhou, and K. Burke, Phys. Rev. Lett. **100**, 136406 (2008).

[47] J. Heyd, G. E. Scuseria, and M. Ernzerhof, J. Chem. Phys. **118**, 8207 (2003).

[48] See Supplemental Material for details about the structure distortions, the ferroelecric and topological properties of superlattices, and the band structure from HSE functional can be found in the Supplemental Material.

[49] I. Souza, N. Marzari, and D. Vanderbilt, Phys. Rev. B **65**, 035109 (2001).

[50] A. A. Mostofi, J. R. Yates, Y.-S. Lee, I. Souza, D. Vanderbilt, and N. Marzari, Comput. Phys. Commun. **178**, 685 (2008).

[51] Q. Wu, S. Zhang, H.-F. Song, M. Troyer, and A. A. Soluyanov, Comput. Phys. Commun. **224**, 405 (2018).

[52] A. M. Glazer, Acta Crystallogr. Sect. B **28**, 33894 (1972).

[53] L. Tao and E. Y. Tsymbal, Nat. Commun. **9**, 1 (2018).

[54] F. Wang, I. Grinberg, and A. M. Rappe, Appl. Phys. Lett. **104**, 152903 (2014).

[55] R. F. Berger, C. J. Fennie, and J. B. Neaton, Phys. Rev. Lett. **107**, 146804 (2011).

[56] D. V. Cirlincione and R. F. Berger, Phys. Rev. B **103**, 045127 (2021).

[57] Y.-H. Meng, W. Bai, H. Gao, S.-J. Gong, J.-Q. Wang, C.-G. Duan, and J.-H. Chu, Nanoscale **9**, 17957 (2017).

[58] E. Plekhanov, P. Barone, D. Di Sante, and S. Picozzi, Phys. Rev. B **90**, 161108(R) (2014).

[59] M. S. Bahramy, B.-J. Yang, R. Arita, and N. Nagaosa, Nat. Commun. **3**, 1 (2012).

[60] M. S. Bahramy, R. Arita, and N. Nagaosa, Phys. Rev. B **84**, 041202(R) (2011).

[61] Y. Xia, D. Qian, D. Hsieh, L.Wray, A. Pal, H. Lin, A. Bansil, D. Grauer, Y. S. Hor, and R. J. Cava *et al.*, Nat. Phys. **5**, 398 (2009).

[62] D. Di Sante, P. Barone, R. Bertacco, and S. Picozzi, Adv. Mater. **25**, 509 (2013).

[63] L. L. Tao, T. R. Paudel, A. A. Kovalev, and E. Y. Tsymbal, Phys. Rev. B **95**, 245141 (2017).

[64] M. Kim, J. Im, A. J. Freeman, J. Ihm, and H. Jin, Proc. Natl. Acad. Sci. USA **111**, 6900 (2014).

Figure Captions

Fig. 1 (a) Atomic structure of $CsSnI_3/CsSiI_3$ superlattice with a space group *Pc*. (b) in-plane polar mode Q_{P_b} made by the ionic motions parallel to the ***b*** direction ($Q_{P_{b,||}}$) and perpendicular to the ***b*** direction ($Q_{P_{b,\perp}}$). The arrows in panel (a) represent the iodine octahedron rotation and tilting. Green, blue, gray, and purple balls represent Cs, Si, Sn, and I atoms, respectively.

Fig. 2 The band structures of $CsSnI_3/CsSiI_3$ superlattice with in-plane polarization of (a) P_b= 12.3 μC/cm^2, (b) P_b= 7.4 μC/cm^2, and (c**)** P_b= 0 μC/cm^2. The red and blue colors represent the corresponding states mainly come from Si/Sn ions and I ions, respectively. In the inset of panel (a), we report the graphical definition of the Rashba momentum offset, k_R, and of the Rashba energy splitting, E_R.

Fig. 3 Bandgap and Rashba parameters of (a) $CsPbI_3/CsSiI_3$ and (b) $CsSnI_3/CsSiI_3$ as a function of the in-plane polarization P_b. The blue and green color contours represent the bandgap.

Fig. 4 Polarization effect on surface states. Band structure of $CsSnI_3/CsSiI_3$ superlattice in a [100] slab geometry with the in-plane polarization of (a) P_b= 6.1 μC/cm^2, (b) P_b= 0 μC/cm^2, and (c) P_b=−6.1 μC/cm^2. The bottom panels of (a)-(c) display the corresponding spin texture of surface states near the Fermi level. (d) The energies of the two Dirac point as a function of P_b. The sketches of the spin texture for Rashba effect with (e) P_b=6.1 μC/cm^2 and (f) P_b=−6.1 μC/cm^2, respectively.

Fig. 5 Bandgap and electronic phase of (a) $CsPbI_3/CsSiI_3$ and (b) $CsSnI_3/CsSiI_3$ superlattice as a function of epitaxial strain. $CsPbI_3/CsSiI_3$ can be NI, TI-E and TI phases depending on the strain. $CsSnI_3/CsSiI_3$ can be TI-E, TI and NI for different strains. Light blue, blue and

green color represent NI, TI-E, and TI phase, respectively. (c) The energies of the Dirac point of surface states of $CsPbI_3/CsSiI_3$ and $CsSnI_3/CsSiI_3$ as a function of strain.

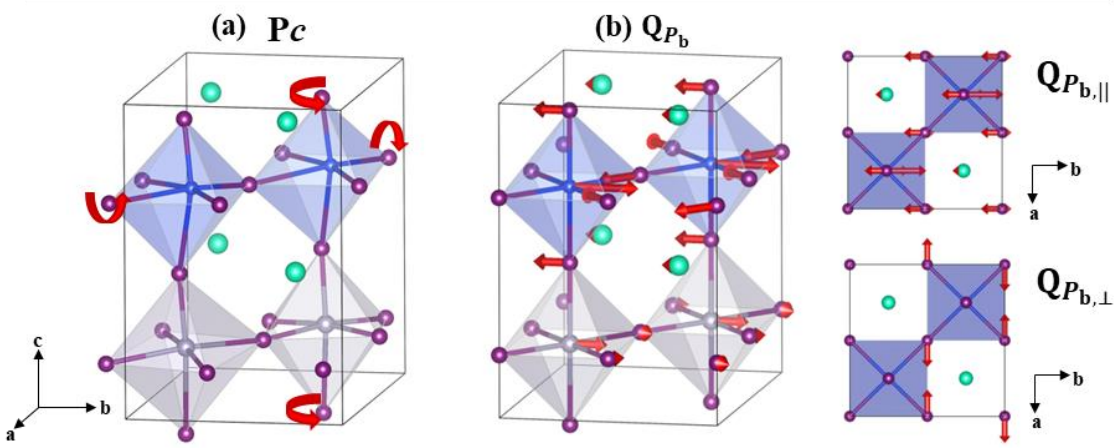

Fig. 1

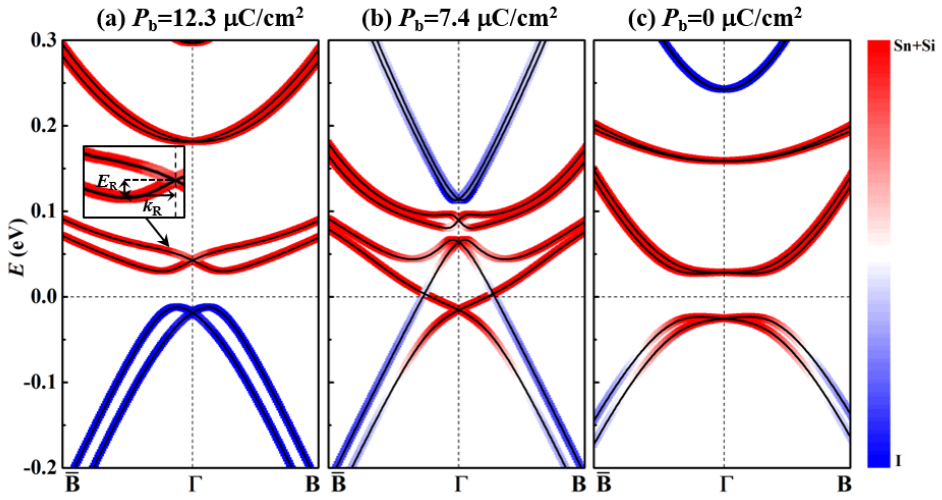

Fig. 2

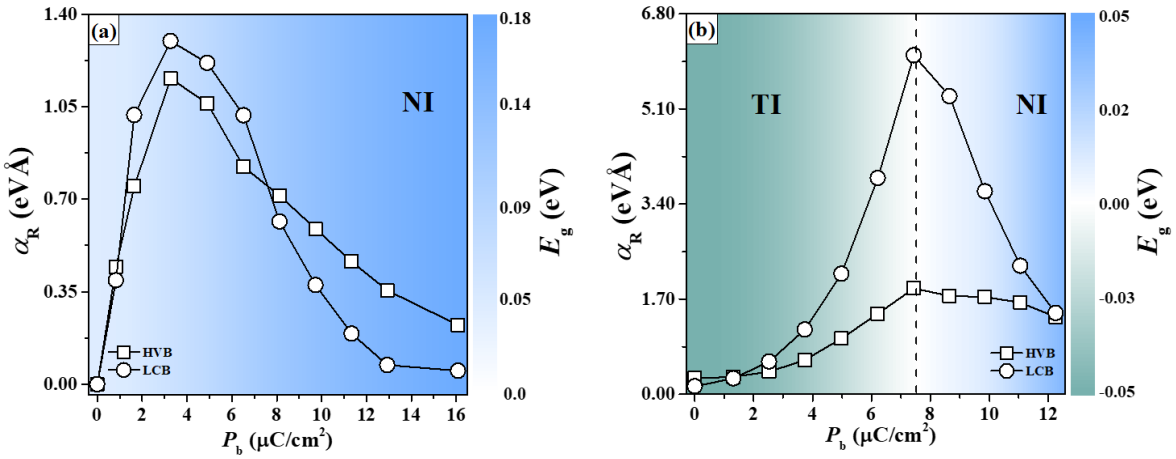
(a)
NI
HVB
LCB
α_R (eVÅ)
E_g (eV)
P_b (μC/cm^2)
(b)
TI
NI
HVB
LCB
α_R (eVÅ)
E_g (eV)
P_b (μC/cm^2)

Fig. 3

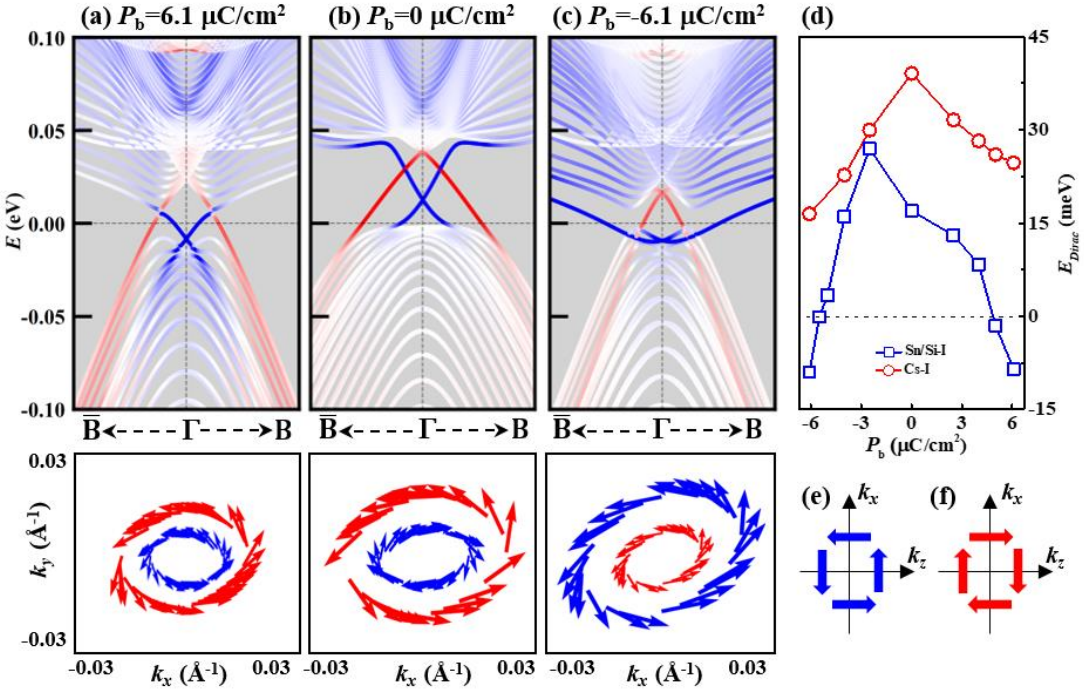
(a) P_b=6.1 μC/cm^2
(b) P_b=0 μC/cm^2
(c) P_b=-6.1 μC/cm^2
(d)
E (eV)
B̄←----Γ----→B
k_y (Å^{-1})
k_x (Å^{-1})
Sn/Si-I
Cs-I
E_{Dirac} (meV)
P_b (μC/cm^2)
(e)
(f)
k_x
k_z

Fig. 4

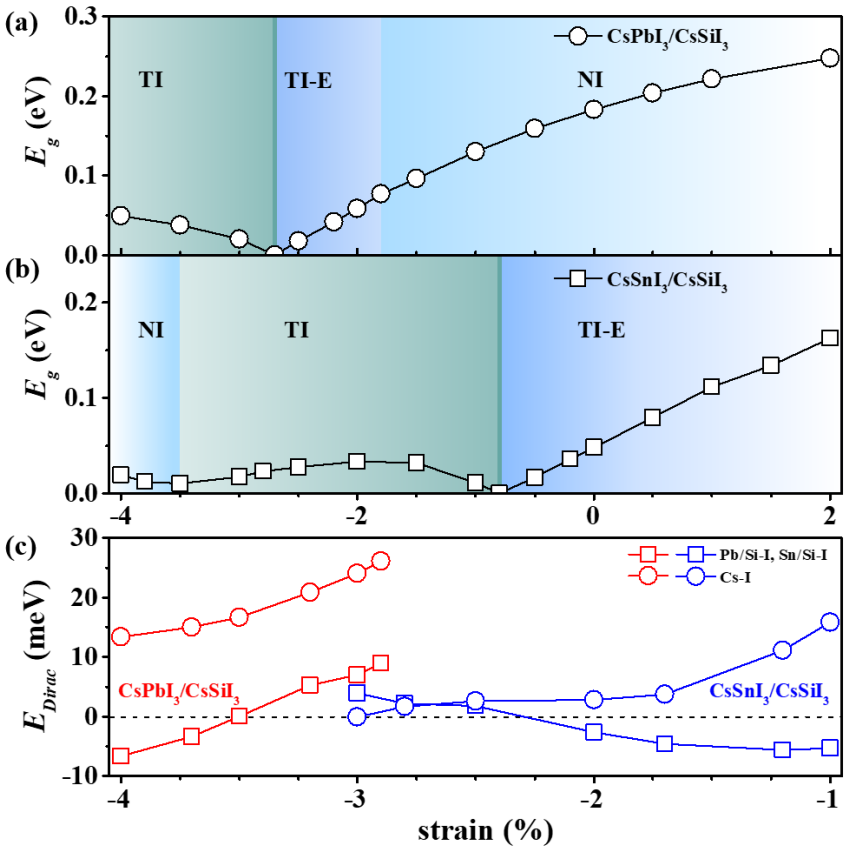
(a)
TI
TI-E
NI
CsPbI3/CsSiI3
Eg (eV)
0.3
0.2
0.1
0.0
(b)
NI
TI
TI-E
CsSnI3/CsSiI3
Eg (eV)
0.2
0.1
0.0
-4
-2
0
2
(c)
Pb/Si-I, Sn/Si-I
Cs-I
CsPbI3/CsSiI3
CsSnI3/CsSiI3
EDirac (meV)
30
20
10
0
-10
-4
-3
-2
-1
strain (%)

Fig. 5